

Semimetal or Semiconductor: The Nature of High Intrinsic Electrical Conductivity in TiS_2

Han Wang,^{†,‡,¶} Zhizhan Qiu,^{§,¶} Weiyi Xia,^{||,¶} Chen Ming,[⊥] Yuyan Han,[#] Liang Cao,[#] Jiong Lu,^{§,¶} Peihong Zhang,^{||} Shengbai Zhang,[†] Hai Xu,^{*,∇,○} and Yi-Yang Sun^{*,⊥,†,¶}

[†]Department of Physics, Applied Physics, and Astronomy, Rensselaer Polytechnic Institute, Troy, New York 12180, United States

[‡]Chemical Sciences Division, Lawrence Berkeley National Laboratory, Berkeley, California 94720, United States

[§]Department of Chemistry, National University of Singapore, Singapore 117543

^{||}Department of Physics, University at Buffalo, State University of New York, Buffalo, New York 14260, United States

[⊥]State Key Laboratory of High Performance Ceramics and Superfine Microstructure, Shanghai Institute of Ceramics, Chinese Academy of Sciences, Shanghai 201899, China

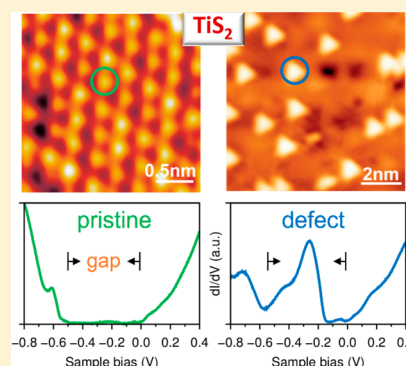
[#]Anhui Province Key Laboratory of Condensed Matter Physics at Extreme Conditions, High Magnetic Field Laboratory of the Chinese Academy of Sciences, Hefei 230031, China

[∇]Changchun Institute of Optics, Fine Mechanics, and Physics, Chinese Academy of Sciences, Changchun 130033, China

[○]Center of Materials Science and Optoelectronics Engineering, University of Chinese Academy of Sciences, Beijing 100049, China

Supporting Information

ABSTRACT: As an intensively studied electrode material for secondary batteries, TiS_2 is known to exhibit high electrical conductivity without extrinsic doping. However, the origin of this high conductivity, either being a semimetal or a heavily self-doped semiconductor, has been debated for several decades. Here, combining quasi-particle GW calculations, density functional theory (DFT) study on intrinsic defects, and scanning tunneling microscopy/spectroscopy (STM/STS) measurements, we conclude that stoichiometric TiS_2 is a semiconductor with an indirect band gap of about 0.5 eV. The high conductivity of TiS_2 is therefore caused by heavy self-doping. Our DFT results suggest that the dominant donor defect that is responsible for the self-doping under thermal equilibrium is Ti interstitial, which is corroborated by our STM/STS measurements.



TiS_2 is the first cathode material successfully used in lithium-ion batteries.¹ Since then, TiS_2 has remained to be actively studied due to its attractive properties. The lithium diffusion coefficient in TiS_2 is on the order of 10^{-8} – 10^{-7} cm^2/s ,^{1–3} significantly higher than that in widely used oxide cathode materials, which is typically on the order of 10^{-9} cm^2/s .^{4–6} A recent experiment demonstrated that TiS_2 cells could retain more than 50% of the original capacity after 35 years of storage, suggesting its high stability.⁷ TiS_2 could also have better compatibility with sulfide solid electrolytes,^{8–10} as well as other solid electrolytes,¹¹ than commonly used oxide cathode materials. When the research interest goes beyond lithium-ion batteries, TiS_2 has been widely explored for secondary batteries using Na,^{12,13} K,¹⁴ and Mg anodes.^{15,16} One of the important reasons that TiS_2 was selected as a cathode material for lithium-ion batteries is that it exhibits high intrinsic electrical conductivity without being extrinsically doped.¹ This is different from some other popular cathode materials, such as LiFePO_4 , for which the low conductivity has been a main issue.^{17,18} Another famous example is the low conductivity of the sulfur cathode in Li–S batteries. Recently,

the high electrical conductivity of TiS_2 has been utilized to encapsulate the sulfur cathode to enhance its conductivity.¹⁹ This work has attracted significant attention as it could also tackle a major obstacle in developing Li–S batteries, i.e., the shuttle effect of polysulfide species.^{20–24} Despite these wide applications, however, the understanding on the origin of the high conductivity of TiS_2 has been elusive so far.

TiS_2 was first suggested to be a semiconductor based on the reflectivity spectrum, and a band gap of 0.9 eV was conjectured by an extrapolation from the band gaps of HfS_2 and ZrS_2 .²⁵ Thompson and co-workers later argued that their data on the Seebeck coefficient and resistivity are much easier to explain if TiS_2 is a metal.²⁶ This opinion was supported by the X-ray band spectrum and infrared reflectance spectrum.^{27,28} However, Friend and co-workers found that, in contrast to TiSe_2 , the Hall coefficient of TiS_2 was nearly independent of pressure, and therefore, a semiconductor picture was favored.²⁹ A band

Received: September 14, 2019

Accepted: October 25, 2019

Published: October 25, 2019

gap of 0.5 eV was proposed by Wilson, but without direct evidence.³⁰ Later, angle-resolved photoemission spectroscopy (ARPES) measurements suggested a band gap of 0.3 eV.^{31,32} However, the ARPES results were soon challenged by density functional theory (DFT) calculation, which yielded a semimetal for stoichiometric TiS₂.³³ Since the 1990s, the opinion that TiS₂ is semimetallic has become prevalent, which is partly because DFT calculations became widely accessible and consistent results on semimetallicity were achieved by different groups.^{34–37} It is noted that, despite the popularity of the semimetallic picture, a band gap of 0.5 eV based on scanning tunneling microscopy/spectroscopy (STM/STS) measurements has been claimed³⁸ but was ignored by the community possibly because of the ambiguity in assigning the measured gap.

To address the controversy on the semimetal or semiconductor nature of bulk TiS₂, it is imperative to understand its defect physics, particularly the dominant defects in this material, which has been similarly inconclusive. Several defects have been considered as candidates. As the material often exhibits nonstoichiometry, it has been assumed that Ti interstitial defects give rise to the free carriers. However, anion vacancies are known to be abundant in transition metal dichalcogenide materials, which may serve as the donor defects too. Other defects such as a Ti Frenkel pair (Ti_F), sometimes called a displacement Ti defect, have also been considered as the cause for the self-doping.^{39–42} TiS₂ has been experimentally shown to exhibit a complex relation between conductivity and temperature,^{43,44} which is directly related to the defect physics of this material. So far, there has been no direct identification of the dominant defects in TiS₂ other than the nonstoichiometry arguments.

In this Letter, we present a successful case study differentiating between the semiconducting and semimetallic nature of a narrow-band-gap material. We clarify the electronic structure of stoichiometric and defective TiS₂ and identify the origin of the high intrinsic electrical conductivity of this material. Using well-converged quasi-particle GW calculations, we show that stoichiometric TiS₂ is a gapped semiconductor. Our low-temperature STM/STS measurement on a single-crystal TiS₂ surface also unambiguously showed a band gap. To understand the high conductivity, we studied the intrinsic defects based on DFT calculation and found that Ti_i had the lowest defect formation energy. Meanwhile, the Ti_i defect was found to be a shallow donor contributing to the conducting electrons. A midgap defect state observed in our STS experiment can be well reproduced by our calculation on the Ti_i defect. Other possible defects discussed in the literature can be ruled out as the dominant donor because their carrier types or electronic structures are inconsistent with experiment. Our work thus concludes the origin of the high electrical conductivity of TiS₂, on which the debates have lasted for over half of a century.

Our many-body perturbation calculations were carried out within the GW approximation⁴⁵ using a local version of the BerkeleyGW package⁴⁶ implementing an accelerated GW method,⁴⁷ which enabled us to perform fully converged GW calculations. The accuracy of this method has been demonstrated for a diverse range of materials.^{47,48} The Hybertsen–Louie generalized plasmon-pole model⁴⁵ was used to extend the static dielectric function to finite frequencies. The Troullier–Martins norm-conserving pseudopotentials⁴⁹ were used for GW calculations. The Ti 3s, 3p, and

3d semicore electrons were included as valence electrons, which are important in GW calculations.⁵⁰ A plane-wave cutoff energy of 200 Ry was used to properly describe these highly localized semicore states using norm-conserving pseudopotentials.

In GW calculations, we used the experimental lattice constants ($a = 3.407$ Å and $c = 5.695$ Å) for the 1T phase TiS₂.⁵¹ Our DFT calculations using various functionals suggest that the conduction band minimum (CBM) and valence band maximum (VBM) appear at the Γ and L points of the Brillouin zone (BZ), respectively. We therefore calculated the band gap between these two points. There are two important truncation parameters imposed in GW calculations that affect the convergence of the results.^{47,52} One is the kinetic energy cutoff for the dielectric matrix; the other is the number of conduction bands included in the dielectric matrix and electron self-energy calculations. Figure 1 shows the con-

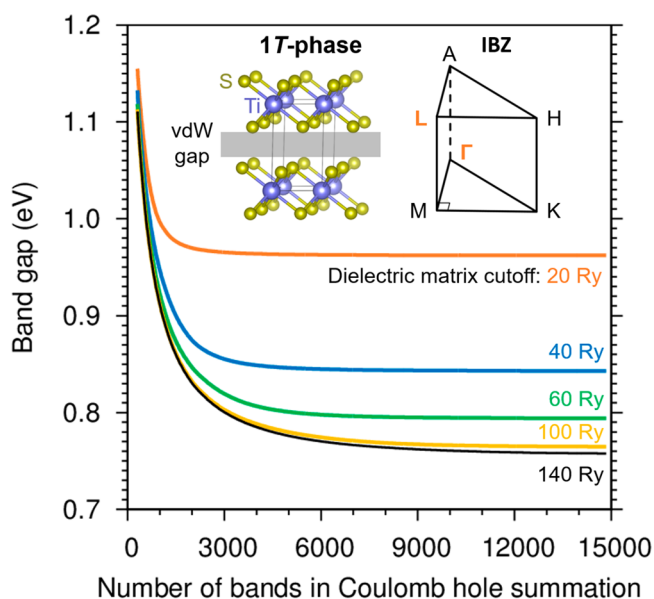


Figure 1. GW band gap of 1T-TiS₂ between the Γ and L points as a function of the number of conduction bands included in the Coulomb-hole self-energy calculation and the cutoff of the dielectric matrix. Insets show the atomic structure (left) and the irreducible BZ. In the atom structure, the gray region shows the vdW gap, where the interstitials reside.

vergence behavior of the calculated GW band gap with respect to the two parameters. The converged band gap is about 0.76 eV, confirming the semiconducting nature of stoichiometric TiS₂. It is worth noting that the calculated band gap decreases with increasing truncation parameters. This behavior is different from that of the GW band gap of s–p gap semiconductors, e.g., ZnO⁵² and CuCl.⁴⁸ This difference is because TiS₂ is a p–d gap semiconductor with the CBM state derived from more localized Ti 3d states.

To verify the calculated band gap, we used low-temperature STM/STS. Our STM experiment was performed using a Createc system. The synthetic 1T-TiS₂ single crystal was purchased from HQ Graphene and was measured to exhibit a relatively high conductivity of 8×10^5 S/m at room temperature with an estimated electron concentration of 10^{21} – 10^{22} /cm³. The composition of the sample was measured to be Ti:S = 1:1.93–1:1.96 by energy-dispersive X-ray

spectroscopy and X-ray photoelectron spectroscopy. The results for characterization of the sample are provided in the Supporting Information (SI). The fresh surface of TiS₂ was prepared by a common tape exfoliating technique, quickly transferred into the preparation chamber (base pressure below 2×10^{-10} mbar), annealed at about 100 °C for 2 h for outgassing, and then cooled down to room temperature before transferring to the analysis chamber (base pressure below 1×10^{-10} mbar) to carry out STM/STS experiments. STS measurements were performed in constant-height mode using a standard lock-in technique ($f = 773$ Hz, $V_{r.m.s.} = 10$ mV). The STM tip was calibrated spectroscopically on the Au(111) surface. All data were collected at 4.5 K.

Figure 2a shows the STM topography of the as-cleaved surface. While a significant amount of defects can be observed

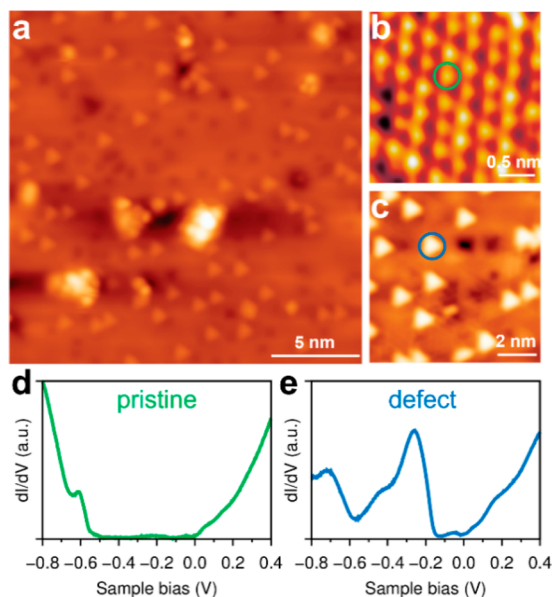


Figure 2. (a) STM topography of the TiS₂ surface ($V_g = 1$ V, $I_t = 100$ pA). (b) Atomically resolved STM image ($V_g = -1$ V, $I_t = 100$ pA) showing a pristine region without the dominant defects. (c) Dominant defects observed on the TiS₂ surface ($V_g = -0.65$ V, $I_t = 100$ pA). (d) dI/dV spectrum recorded at a point marked by a green circle in (b). (e) dI/dV spectrum recorded on a defect marked by a blue circle in (c).

on the surface, we take the advantage that the STS measurement can detect the local electronic structure by avoiding the areas occupied by defects. Figure 2b shows a relatively clean region on the surface showing atomic resolution. The lattice constant a_0 is measured to be 3.4 ± 0.1 Å, consistent with previous diffraction experiments. We recorded the dI/dV spectrum at the point marked by a circle in Figure 2b. The spectrum is shown in Figure 2d, where a clear band gap of about 0.5 eV can be seen. Meanwhile, the Fermi level (0 eV in the spectrum) is close to the onset of the conduction band, suggesting a strong n-type conductivity. The clear band gap seen in Figure 2d, which is consistent with our GW calculation, leads us to conclude that stoichiometric TiS₂ is a semiconductor. Our current GW method may overestimate the band gap to some extent. Other effects such as the electron–phonon renormalization⁵³ could also lead to a reduced apparent band gap as measured by STS.

Accepting the semiconducting nature of stoichiometric TiS₂, we next address the issue of the origin of its high conductivity. So far, the assignment of the defect that is responsible for the high conductivity has been exclusively based on indirect evidence with no knowledge of the electronic structure of the defects. Here, we study the properties of intrinsic defects in TiS₂ based on DFT calculations. Our calculations were carried out with the Vienna Ab initio Simulation Package (VASP),⁵⁴ where the interaction between ion cores and valence electrons was described by the projector-augmented wave (PAW) method.⁵⁵ We used the newly developed SCAN-rVV10 functional.^{56,57} A Hubbard U value of 2.1 eV for Ti 3d orbitals derived from first-principles calculation⁵⁸ was added on top of the SCAN-rVV10 functional. The optimized lattice constants ($a = 3.434$ Å and $c = 5.685$ Å) using a plane-wave cutoff of 40 Ry and $10 \times 10 \times 6$ k -points in the BZ are in good agreement with experimental values. The calculated band gap with the SCAN-rVV10+ U method was 0.47 eV, consistent with our STS measurement.

We calculated the formation energy (E^{form}) of a defect following the standard approach^{59,60}

$$E^{\text{form}} = E_D^q - E_0 + \sum_i n_i \mu_i + q(E_{\text{VBM}} + E_F)$$

where E_D^q is the total energy of the defect-containing supercell with charge q , E_0 is the total energy of the defect-free supercell, E_F is the Fermi energy measured from the VBM, E_{VBM} , μ_i is the chemical potential of element i , and n_i is the number of atoms changed during the formation of the defect. The chemical potentials, μ_{Ti} and μ_{S} , are calculated with respect to the total energy per atom (E_i) in corresponding bulk phases of Ti and S, i.e., $\mu_i = \mu_i' + E_i$. The allowed range for the chemical potentials is determined by satisfying $\mu_{\text{Ti}} + 2\mu_{\text{S}} = \Delta E(\text{TiS}_2)$, where $\Delta E(\text{TiS}_2)$ is the formation energy of TiS₂ from Ti metal in the hcp phase and bulk sulfur in the orthorhombic α phase.⁶¹ $\Delta E(\text{TiS}_2)$ is calculated to be -4.67 eV per formula unit, slightly higher than the experimental value of -4.25 eV.⁶² The allowed range for the chemical potentials is also limited by other possible Ti–S compounds, such as TiS⁶³ and TiS₃.⁶⁴ As shown in Figure 3a, under Ti-rich conditions, monosulfide TiS is thermodynamically more stable than TiS₂, while TiS₃ is only a metastable phase in our SCAN-rVV10+ U calculation.

The calculated defect formation energies as a function of chemical potential are shown in Figure 3b, where we studied the vacancies and interstitials of Ti and S, the S-on-Ti antisite (S_{Ti}), and the Ti Frenkel pair. A $4 \times 4 \times 2$ supercell, a $2 \times 2 \times 2$ k -point grid, and a plane-wave cutoff of 20 Ry were used in these calculations. All atoms were fully relaxed until the forces were smaller than 0.01 eV/Å. Because the Ti-on-S antisite is not stable and relaxes to a pair of Ti_i and V_S, we did not consider it as a stand-alone defect. From Figure 3b, it can be seen that the Ti_i defect has the lowest formation energy, almost regardless of the chemical potential, except for extremely S-rich (Ti-poor) conditions. At highly Ti-rich conditions, the formation energy could become negative, suggesting that formation of Ti_i defects is spontaneous under such conditions. The strong tendency to form Ti_i defects can be attributed to the vdW gap between TiS₂ trilayers. The chemical environment of an interstitial Ti atom between the trilayers is almost the same as that in the center of a trilayer, i.e., octahedral coordination. The Ti–S bond length around the Ti_i defect is 2.46 Å, similar to that in bulk (2.43 Å).

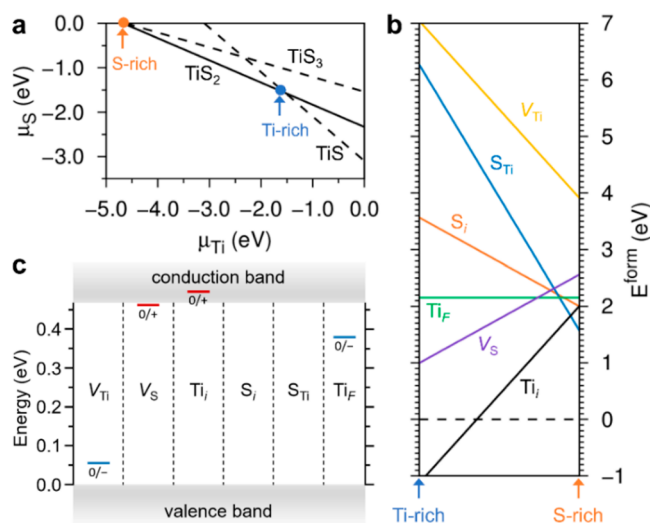


Figure 3. (a) Calculated thermodynamically stable region of TiS_2 with respect to TiS and TiS_3 as a function of the chemical potential of Ti (μ_{Ti}) and S (μ_{S}). (b) Formation energy of intrinsic defects in bulk TiS_2 under the condition from Ti-rich to S-rich, as marked in (a). The considered defects include vacancies (V_{Ti} and V_{S}), interstitials (Ti_{i} and S_{i}), S substitution on Ti (S_{Ti}), and a Ti Frenkel pair (Ti_{F}). (c) Acceptor transition levels $\epsilon(0/-)$, marked by blue bars, and donor transition levels $\epsilon(0/+)$, marked by red bars, calculated using a $7 \times 7 \times 4$ supercell. The S_{i} and S_{Ti} defects do not have defect transition levels within the band gap.

Given the low formation energy of the Ti_{i} defect, it is straightforward to relate the most abundant defects observed on the surface in Figure 2a to this defect. The line profile on the defects (shown in the SI) indeed shows that the defects are higher than (or protruding from) the surface S atoms. To provide evidence on this assignment, we recorded dI/dV spectra on the dominant defects. Figure 2c shows a zoom-in view of a relatively defect-rich region. Figure 2e shows the dI/dV spectrum recorded on the defect marked by a circle in Figure 2c. From this spectrum, a prominent defect-derived peak is observed in the band gap, which is located at about -0.25 eV. As the dI/dV spectrum is directly related to the density of states (DOS), we calculated the DOS for all defects in order to identify the origin of this midgap peak.

Figure 4a shows the DOS plots for all of the defects considered in Figure 3b. It can be seen that only the Ti_{i} defect generates a clear midgap state. By inspecting the partial charge density of the midgap state, as shown in Figure 4b, we see that this state is contributed to by a bonding state between the d_{z^2} orbitals of the Ti_{i} defect atom and its two neighboring Ti atoms in the trilayers. The bonding state brings two electrons of the Ti_{i} atom from the conduction band to the midgap. The other two electrons of the Ti_{i} atom remain in the conduction band. With a reasonable concentration of Ti_{i} defects, this gap state can have significant dispersion, as shown in Figure 4c, the band structure plot of the $4 \times 4 \times 2$ supercell containing a Ti_{i} defect. The dispersion of the defect band results in a broad peak in the DOS plot. In contrast, none of the other defects generate a midgap state. We also checked the case with a Ti atom staying on the surface. The DOS plot is shown in the SI, where a similar band gap defect state can also be seen. Thus, the dominant defects as observed by STM can be evidently assigned to the Ti_{i} defects.

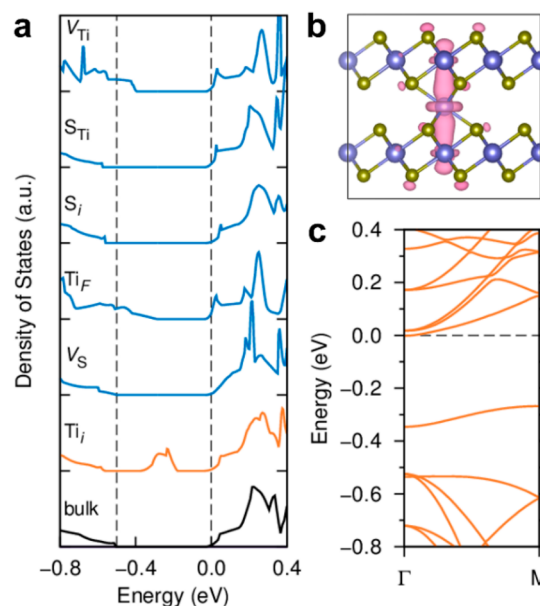


Figure 4. (a) DOS for bulk TiS_2 and intrinsic defects as calculated using a $4 \times 4 \times 2$ supercell. The dashed lines mark the VBM and CBM of bulk. (b) Charge density plot of the midgap state of the Ti_{i} defect. (c) Band structure plot for the Ti_{i} defect in a $4 \times 4 \times 2$ supercell.

Finally, we studied the defect transition levels to check whether the Ti_{i} defect is a shallow donor. To avoid large errors associated with high charge states, we only studied $(0/+)$ and $(0/-)$ transitions using a much larger $7 \times 7 \times 4$ supercell, which are sufficient to demonstrate the shallowness of a defect. Γ -point sampling of the BZ was used in these calculations. The defect transition level from charge state q to q' were calculated according to $\epsilon(q/q') = [(E_{\text{B}}^q - E_{\text{B}}^{q'}) / (q - q')] - E_{\text{VBM}}$. As shown in Figure 3c, the Ti_{i} defect has its $\epsilon(0/+)$ transition level above the CBM, suggesting that Ti_{i} defect is indeed a shallow donor. V_{S} is also a shallow donor. However, due to its relatively high formation energy, as shown in Figure 3b, and hence low concentration, it may not serve as the dominant donor defect in TiS_2 under thermal equilibrium growth conditions. The Ti Frenkel pair (Ti_{F}) is another defect that has been widely discussed in the literature.^{39,41,42} However, our calculation shows that its formation energy (above 2 eV using a $4 \times 4 \times 2$ supercell) is high enough to prevent it from forming in a significant amount. In addition, the Ti Frenkel pair is found to be a deep acceptor (see Figure 3c). Our results thus exclude the possibility that the Ti Frenkel pair is the dominant donor defect in TiS_2 .

In summary, on the basis of GW and SCAN-rVV10+U calculations and STM/STS experiment, we studied the electronic structure of stoichiometric and defective TiS_2 . We conclude that stoichiometric TiS_2 is an indirect-gap semiconductor with a band gap of about 0.5 eV. Its high conductivity is therefore a result of intrinsic defects instead of semimetallicity. Our calculation and experimental results on the observed midgap defect state, low defect formation energy, and shallow donor transition level all converge to the conclusion that the dominant electron carrier contributor in TiS_2 is the Ti interstitial defects. Other possible defects such as Ti Frenkel pairs and S vacancies should not play an important role. With these results, the origin of the high intrinsic

electrical conductivity of TiS_2 , a property widely employed in the secondary battery community, is considered understood.

■ ASSOCIATED CONTENT

Supporting Information

The Supporting Information is available free of charge on the ACS Publications website at DOI: 10.1021/acs.jpcllett.9b02710.

Experimental characterization of the TiS_2 crystal sample by Hall measurements, X-ray energy dispersion spectrum, and X-ray photoelectron spectrum (PDF)

■ AUTHOR INFORMATION

Corresponding Authors

*E-mail: yysun@mail.sic.ac.cn (Y.-Y.S.).

*E-mail: xuhai@ciomp.ac.cn (H.X.).

ORCID

Liang Cao: 0000-0001-7453-7060

Jiong Lu: 0000-0002-3690-8235

Yi-Yang Sun: 0000-0002-0356-2688

Author Contributions

[¶]H.W., Z.Q., and W.X. contributed equally to this work.

Notes

The authors declare no competing financial interest.

■ ACKNOWLEDGMENTS

Y.-Y.S., who conceived and coordinated the research, acknowledges support by the National Natural Science Foundation of China (NSFC) under Grant 11774365. H.X., Y.H., and L.C. acknowledge support from the NSFC (Grant Nos. 11774341, 11604344, 11574317, and 21503233), and H.X. thanks the 100 Talents Program of the Chinese Academy of Sciences. H.W. and S.B.Z. were supported by the National Science Foundation (NSF) under Award CBET-1510948. P.Z. was supported by the NSF under Award DMR-1506669. We acknowledge the computational support provided by the National Energy Research Scientific Computing Center (NERSC) under support by the Department of Energy Contract DE-AC02-05CH11231 and Stampede supercomputer resources at TACC made available by Extreme Science and Engineering Discovery Environment (XSEDE) through allocation TG-DMR180114, which is supported by National Science Foundation Grant Number ACI-1548562. The authors thank beamline BL11U at NSRL for sample characterization.

■ REFERENCES

- Whittingham, M. S. Electrical Energy Storage and Intercalation Chemistry. *Science* **1976**, *192* (4244), 1126–1127.
- Whittingham, M. S. Chemistry of Intercalation Compounds: Metal Guests in Chalcogenide Hosts. *Prog. Solid State Chem.* **1978**, *12* (1), 41–99.
- Schoonman, J.; Hagenmuller, P. H. B. P.; Van Gool, W. *Solid Electrolytes*; Academic Press: New York, 1978.
- Wang, B.; Bates, J. B.; Hart, F. X.; Sales, B. C.; Zuhr, R. A.; Robertson, J. D. Characterization of Thin-Film Rechargeable Lithium Batteries with Lithium Cobalt Oxide Cathodes. *J. Electrochem. Soc.* **1996**, *143* (10), 3203–3213.
- Striebel, K. A.; Deng, C. Z.; Wen, S. J.; Cairns, E. J. Electrochemical Behavior of LiMn_2O_4 and LiCoO_2 Thin Films Produced with Pulsed Laser Deposition. *J. Electrochem. Soc.* **1996**, *143* (6), 1821–1827.

(6) Prossini, P. P.; Lisi, M.; Zane, D.; Pasquali, M. Determination of the Chemical Diffusion Coefficient of Lithium in LiFePO_4 . *Solid State Ionics* **2002**, *148* (1–2), 45–51.

(7) Pereira, N.; Amatucci, G. G.; Whittingham, M. S.; Hamlen, R. Lithium–Titanium Disulfide Rechargeable Cell Performance after 35 Years of Storage. *J. Power Sources* **2015**, *280*, 18–22.

(8) Shin, B. R.; Nam, Y. J.; Oh, D. Y.; Kim, D. H.; Kim, J. W.; Jung, Y. S. Comparative Study of $\text{TiS}_2/\text{Li-In}$ All-Solid-State Lithium Batteries Using Glass-Ceramic Li_3PS_4 and $\text{Li}_{10}\text{GeP}_2\text{S}_{12}$ Solid Electrolytes. *Electrochim. Acta* **2014**, *146*, 395–402.

(9) Oh, D. Y.; Choi, Y. E.; Kim, D. H.; Lee, Y.-G.; Kim, B.-S.; Park, J.; Sohn, H.; Jung, Y. S. All-Solid-State Lithium-Ion Batteries with TiS_2 Nanosheets and Sulphide Solid Electrolytes. *J. Mater. Chem. A* **2016**, *4* (26), 10329–10335.

(10) Trevey, J. E.; Stoldt, C. R.; Lee, S.-H. High Power Nanocomposite TiS_2 Cathodes for All-Solid-State Lithium Batteries. *J. Electrochem. Soc.* **2011**, *158* (12), A1282–A1289.

(11) Unemoto, A.; Ikeshoji, T.; Yasaku, S.; Matsuo, M.; Stavila, V.; Udovic, T. J.; Orimo, S. Stable Interface Formation between TiS_2 and LiBH_4 in Bulk-Type All-Solid-State Lithium Batteries. *Chem. Mater.* **2015**, *27* (15), 5407–5416.

(12) Bian, X.; Gao, Y.; Fu, Q.; Indris, S.; Ju, Y.; Meng, Y.; Du, F.; Bramnik, N.; Ehrenberg, H.; Wei, Y. A Long Cycle-Life and High Safety $\text{Na}^+/\text{Mg}^{2+}$ Hybrid-Ion Battery Built by Using a TiS_2 Derived Titanium Sulfide Cathode. *J. Mater. Chem. A* **2017**, *5* (2), 600–608.

(13) Liu, Y.; Wang, H.; Cheng, L.; Han, N.; Zhao, F.; Li, P.; Jin, C.; Li, Y. TiS_2 Nanoplates: A High-Rate and Stable Electrode Material for Sodium Ion Batteries. *Nano Energy* **2016**, *20*, 168–175.

(14) Tian, B.; Tang, W.; Leng, K.; Chen, Z.; Tan, S. J. R.; Peng, C.; Ning, G.-H.; Fu, W.; Su, C.; Zheng, G. W.; et al. Phase Transformations in TiS_2 during K Intercalation. *ACS Energy Lett.* **2017**, *2* (8), 1835–1840.

(15) Sun, X.; Bonnick, P.; Nazar, L. F. Layered TiS_2 Positive Electrode for Mg Batteries. *ACS Energy Lett.* **2016**, *1* (1), 297–301.

(16) Yoo, H. D.; Liang, Y.; Dong, H.; Lin, J.; Wang, H.; Liu, Y.; Ma, L.; Wu, T.; Li, Y.; Ru, Q.; et al. Fast Kinetics of Magnesium Monochloride Cations in Interlayer-Expanded Titanium Disulfide for Magnesium Rechargeable Batteries. *Nat. Commun.* **2017**, *8*, 339.

(17) Chung, S. Y.; Bloking, J. T.; Chiang, Y. M. Electronically Conductive Phospho-Olivines as Lithium Storage Electrodes. *Nat. Mater.* **2002**, *1* (2), 123–128.

(18) Tarascon, J. M.; Armand, M. Issues and Challenges Facing Rechargeable Lithium Batteries. *Nature* **2001**, *414* (6861), 359–367.

(19) Seh, Z. W.; Yu, J. H.; Li, W.; Hsu, P.-C.; Wang, H.; Sun, Y.; Yao, H.; Zhang, Q.; Cui, Y. Two-Dimensional Layered Transition Metal Disulphides for Effective Encapsulation of High-Capacity Lithium Sulphide Cathodes. *Nat. Commun.* **2014**, *5*, 5017.

(20) Ma, L.; Wei, S.; Zhuang, H. L.; Hendrickson, K. E.; Hennig, R. G.; Archer, L. A. Hybrid Cathode Architectures for Lithium Batteries Based on TiS_2 and Sulfur. *J. Mater. Chem. A* **2015**, *3* (39), 19857–19866.

(21) Ma, L.; Hendrickson, K. E.; Wei, S.; Archer, L. A. Nanomaterials: Science and Applications in the Lithium-Sulfur Battery. *Nano Today* **2015**, *10* (3), 315–338.

(22) Pang, Q.; Liang, X.; Kwok, C. Y.; Nazar, L. F. Advances in Lithium-Sulfur Batteries Based on Multifunctional Cathodes and Electrolytes. *Nat. Energy* **2016**, *1*, 16132.

(23) Sun, Y.; Liu, N.; Cui, Y. Promises and Challenges of Nanomaterials for Lithium-Based Rechargeable Batteries. *Nat. Energy* **2016**, *1*, 16071.

(24) Liu, X.; Huang, J.-Q.; Zhang, Q.; Mai, L. Nanostructured Metal Oxides and Sulfides for Lithium-Sulfur Batteries. *Adv. Mater.* **2017**, *29* (20), 1601759.

(25) Greenaway, D. L.; Nitsche, R. Preparation and Optical Properties of Group IV–VI₂ Chalcogenides Having the CdI_2 Structure. *J. Phys. Chem. Solids* **1965**, *26* (9), 1445–1458.

(26) Thompson, A. H.; Pisharody, K. R.; Koehler, R. F. Experimental Study of Solid Solutions $\text{Ti}_x\text{Ta}_{1-x}\text{S}_2$. *Phys. Rev. Lett.* **1972**, *29* (3), 163–166.

- (27) Lucovsky, G.; White, R. M.; Benda, J. A.; Revelli, J. F. Infrared-Reflectance Spectra of Layered Group-IV and Group-VI Transition-Metal Dichalcogenides. *Phys. Rev. B* **1973**, *7* (8), 3859–3870.
- (28) Fischer, D. W. X-Ray Band Spectra and Electronic Structure of TiS_2 . *Phys. Rev. B* **1973**, *8* (8), 3576–3582.
- (29) Friend, R. H.; Jérôme, D.; Liang, W. Y.; Mikkelsen, C.; Yoffe, A. D. Semimetallic Character of TiSe_2 and Semiconductor Character of TiS_2 under Pressure. *J. Phys. C: Solid State Phys.* **1977**, *10* (24), L705–L708.
- (30) Wilson, J. A. Concerning the Semimetallic Characters of TiS_2 and TiSe_2 . *Solid State Commun.* **1977**, *22* (9), 551–553.
- (31) Chen, C. H.; Fabian, W.; Brown, F. C.; Woo, K. C.; Davies, B.; DeLong, B.; Thompson, A. H. Angle-Resolved Photoemission Studies of the Band Structure of TiSe_2 and TiS_2 . *Phys. Rev. B: Condens. Matter Mater. Phys.* **1980**, *21* (2), 615–624.
- (32) Barry, J. J.; Hughes, H. P.; Klipstein, P. C.; Friend, R. H. Stoichiometry Effects in Angle-Resolved Photoemission and Transport Studies of $\text{Ti}_{1+x}\text{S}_2$. *J. Phys. C: Solid State Phys.* **1983**, *16* (2), 393–402.
- (33) Umrigar, C.; Ellis, D. E.; Wang, D.; Krakauer, H.; Posternak, M. Band Structure, Intercalation, and Interlayer Interactions of Transition-Metal Dichalcogenides: TiS_2 and LiTiS_2 . *Phys. Rev. B: Condens. Matter Mater. Phys.* **1982**, *26* (9), 4935–4950.
- (34) Liu, B.; Yang, J.; Han, Y.; Hu, T.; Ren, W.; Liu, C.; Ma, Y.; Gao, C. Electronic Structure of TiS_2 and Its Electric Transport Properties under High Pressure. *J. Appl. Phys.* **2011**, *109* (5), 053717.
- (35) Sharma, S.; Nautiyal, T.; Singh, G. S.; Auluck, S.; Blaha, P.; Ambrosch-Draxl, C. Electronic Structure of 1T- TiS_2 . *Phys. Rev. B: Condens. Matter Mater. Phys.* **1999**, *59* (23), 14833–14836.
- (36) Wu, Z. Y.; Lemoigno, F.; Gressier, P.; Ouvrard, G.; Moreau, P.; Rouxel, J.; Natoli, C. R. Experimental and Theoretical Studies of the Electronic Structure of TiS_2 . *Phys. Rev. B: Condens. Matter Mater. Phys.* **1996**, *54* (16), R11009–R11013.
- (37) Fang, C. M.; de Groot, R. A.; Haas, C. Bulk and Surface Electronic Structure of 1T- TiS_2 and 1T- TiSe_2 . *Phys. Rev. B: Condens. Matter Mater. Phys.* **1997**, *56* (8), 4455–4463.
- (38) Wang, C.; Dotson, L.; Mckelvy, M.; Glaunsinger, W. Scanning Tunneling Spectroscopy Investigation of Charge Transfer in Model Intercalation Compounds $\text{Ti}_{1+x}\text{S}_2$. *J. Phys. Chem.* **1995**, *99* (20), 8216–8221.
- (39) Kukkonen, C. A.; Kaiser, W. J.; Logothetis, E. M.; Blumenstock, B. J.; Schroeder, P. A.; Faile, S. P.; Colella, R.; Gambold, J. Transport and Optical Properties of $\text{Ti}_{1+x}\text{S}_2$. *Phys. Rev. B: Condens. Matter Mater. Phys.* **1981**, *24* (4), 1691–1709.
- (40) Phillips, J. C. High-Temperature Superconductivity in Bridge and Layer Compounds. *Phys. Rev. Lett.* **1972**, *28* (18), 1196–1198.
- (41) Takeuchi, S.; Katsuta, H. Electric and Magnetic Properties of Non-Stoichiometric TiS_2 Phase. *Nippon Kinzoku Gakkaishi* **1970**, *34* (7), 764–771.
- (42) Wilson, J. A. Modeling Contrasting Semimetallic Characters of TiS_2 and TiSe_2 . *Phys. Status Solidi B* **1978**, *86* (1), 11–36.
- (43) Thompson, A. H. Electron-Electron Scattering in TiS_2 . *Phys. Rev. Lett.* **1975**, *35* (26), 1786–1789.
- (44) Kukkonen, C. A.; Maldague, P. F. Electron-Hole Scattering and Electrical-Resistivity of Semimetal TiS_2 . *Phys. Rev. Lett.* **1976**, *37* (12), 782–785.
- (45) Hybertsen, M. S.; Louie, S. G. Electron Correlation in Semiconductors and Insulators: Band Gaps and Quasiparticle Energies. *Phys. Rev. B: Condens. Matter Mater. Phys.* **1986**, *34* (8), 5390–5413.
- (46) Deslippe, J.; Samsonidze, G.; Strubbe, D. A.; Jain, M.; Cohen, M. L.; Louie, S. G. BerkeleyGW: A Massively Parallel Computer Package for the Calculation of the Quasiparticle and Optical Properties of Materials and Nanostructures. *Comput. Phys. Commun.* **2012**, *183* (6), 1269–1289.
- (47) Gao, W.; Xia, W.; Gao, X.; Zhang, P. Speeding up GW Calculations to Meet the Challenge of Large Scale Quasiparticle Predictions. *Sci. Rep.* **2016**, *6*, 36849.
- (48) Gao, W.; Xia, W.; Wu, Y.; Ren, W.; Gao, X.; Zhang, P. Quasiparticle Band Structures of CuCl , CuBr , AgCl , and AgBr : The Extreme Case. *Phys. Rev. B: Condens. Matter Mater. Phys.* **2018**, *98* (4), 045108.
- (49) Troullier, N.; Martins, J. L. Efficient Pseudopotentials for Plane-Wave Calculations. *Phys. Rev. B: Condens. Matter Mater. Phys.* **1991**, *43* (3), 1993–2006.
- (50) Rohlffing, M.; Krüger, P.; Pollmann, J. Quasiparticle Band Structure of CdS . *Phys. Rev. Lett.* **1995**, *75* (19), 3489–3492.
- (51) Chianelli, R. R.; Scanlon, J. C.; Thompson, A. H. Structure Refinement of Stoichiometric TiS_2 . *Mater. Res. Bull.* **1975**, *10* (12), 1379–1382.
- (52) Shih, B.-C.; Xue, Y.; Zhang, P.; Cohen, M. L.; Louie, S. G. Quasiparticle Band Gap of ZnO : High Accuracy from the Conventional G0W0 Approach. *Phys. Rev. Lett.* **2010**, *105* (14), 146401.
- (53) Alawadhi, H.; Tsoi, S.; Lu, X.; Ramdas, A. K.; Grimsditch, M.; Cardona, M.; Lauck, R. Effect of Temperature on Isotopic Mass Dependence of Excitonic Band Gaps in Semiconductors: ZnO . *Phys. Rev. B: Condens. Matter Mater. Phys.* **2007**, *75* (20), 205207.
- (54) Kresse, G.; Furthmüller, J. Efficiency of Ab-Initio Total Energy Calculations for Metals and Semiconductors Using a Plane-Wave Basis Set. *Comput. Mater. Sci.* **1996**, *6* (1), 15–50.
- (55) Kresse, G.; Joubert, D. From Ultrasoft Pseudopotentials to the Projector Augmented-Wave Method. *Phys. Rev. B: Condens. Matter Mater. Phys.* **1999**, *59* (3), 1758–1775.
- (56) Sun, J.; Remsing, R. C.; Zhang, Y.; Sun, Z.; Ruzsinszky, A.; Peng, H.; Yang, Z.; Paul, A.; Waghmare, U.; Wu, X.; Klein, M. L.; Perdew, J. P. Accurate First-Principles Structures and Energies of Diverse Bonded Systems from an Efficient Density Functional. *Nat. Chem.* **2016**, *8*, 831–836.
- (57) Peng, H.; Yang, Z.-H.; Perdew, J. P.; Sun, J. Versatile van Der Waals Density Functional Based on a Meta-Generalized Gradient Approximation. *Phys. Rev. X* **2016**, *6* (4), 041005.
- (58) Sánchez, K.; Palacios, P.; Wahnón, P. Electronic Structure of Bulk- and Na-Intercalated TiS_2 Determined from a GGA+U Study with the Hubbard Terms Obtained Ab Initio. *Phys. Rev. B: Condens. Matter Mater. Phys.* **2008**, *78* (23), 235121.
- (59) Freysoldt, C.; Grabowski, B.; Hickel, T.; Neugebauer, J.; Kresse, G.; Janotti, A.; Van de Walle, C. G. First-Principles Calculations for Point Defects in Solids. *Rev. Mod. Phys.* **2014**, *86* (1), 253–305.
- (60) Zhang, S. B.; Northrup, J. E. Chemical Potential Dependence of Defect Formation Energies in GaAs: Application to Ga Self-Diffusion. *Phys. Rev. Lett.* **1991**, *67* (17), 2339–2342.
- (61) Rettig, S. J.; Trotter, J. Refinement of the Structure of Orthorhombic Sulfur, α -S8. *Acta Crystallogr., Sect. C: Cryst. Struct. Commun.* **1987**, *43* (12), 2260–2262.
- (62) O'Hare, P. A. G.; Johnson, G. K. Thermochemistry of Inorganic Sulfur Compounds VII. Standard Molar Enthalpy of Formation at 298.15 K, High-Temperature Enthalpy Increments, and Other Thermodynamic Properties to 1100 K of Titanium Disulfide, TiS_2 . *J. Chem. Thermodyn.* **1986**, *18* (2), 189–199.
- (63) Schönberg, N. The Tungsten Carbide and Nickel Arsenide Structures. *Acta Metall.* **1954**, *2* (3), 427–432.
- (64) Furuse, S.; Brattås, L.; Kjekshus, A.; Andresen, A. F.; Fischer, P. On the Crystal Structures of TiS_3 , ZrS_3 , ZrSe_3 , ZrTe_3 , HfS_3 , and HfSe_3 . *Acta Chem. Scand.* **1975**, *29a*, 623–631.